Journal of Zhejiang University-SCIENCE A 2026 27(7):730-745
www.jzus.zju.edu.cn; www.springer.com/journal/11582
E-mail: jzus_a@zju.edu.cn

Research Article
https://doi.org/10.1631/jzus.A2500674

Check for updates

Bond of rebar to crumb rubber concrete (CRC) under fiber-reinforced polymer (FRP)–stirrup dual confinement: failure mechanism and behavior modeling

Qiang LI[1], Fangduo XIAO[2]✉, Shiwei LU[3], Jizhong WANG[4], Shikun CHEN[2], Dongming YAN[2]✉

[1]*College of Civil Engineering and Architecture, Zhejiang University of Water Resources and Electric Power, Hangzhou 310018, China*
[2]*College of Civil Engineering and Architecture, Zhejiang University, Hangzhou 310058, China*
[3]*School of Civil Engineering, Yantai University, Yantai 264005, China*
[4]*State Key Laboratory of Coastal and Offshore Engineering, Dalian University of Technology, Dalian 116024, China*

Abstract: The replacement of traditional aggregates with recycled rubber in concrete is increasingly attractive, driven by sustainability-related considerations. Nevertheless, incorporating rubber particles alters both the microinterfacial characteristics and the macroscopic performance of concrete, which leads to the variation in bond behavior between rebar and rubberized concrete. Against this background, 42 central pull-out specimens were prepared for bond tests, and the impact of the rubber replacement ratio (ρ_{rv}) on the bond behavior was investigated. Moreover, specimens with different confined conditions were designed to identify a reliable strengthening scheme for crumb rubber concrete (CRC) members. The test results show that when ρ_{rv} increases from 0% to 30%, the crack width of the splitting specimens decreases, but the bond strength deteriorates simultaneously. When ρ_{rv} increases to 40%, the specimens are subjected to pull-out failure, and the deterioration of the bond strength can be alleviated. Specimens strengthened by fiber-reinforced polymer (FRP) and/or stirrups undergo pull-out failure and exhibit higher bond strength than that of their unstrengthened counterparts. Confinement enhances the bond strength of CRC specimens, beyond which further confinement induces no additional gains. By calibrating rubber-influenced parameters and the confinement critical effect, a mechanics-based model is established for predicting the bond strength of the CRC–rebar interface. Finally, the stochasticity of the bond–slip response is simulated based on the assumption of multi-composite spring–friction units fracturing stochastically, and a continuous bond–slip model with high accuracy and an integral absolute error (E_{IA}) below 10.47% is proposed.

Key words: Crumb rubber concrete (CRC); Rubber replacement ratio (ρ_{rv}); Bond strength model; Fiber-reinforced polymer (FRP)–stirrup confinement; Bond–slip model

1 Introduction

Numerous waste tires are produced annually (Azevedo et al., 2012), and the majority are disposed of in landfills (Ferdous et al., 2021). However, the long-term accumulation of waste rubber not only occupies land but also releases poisonous chemicals, causing pollution of soil and groundwater (Zhang et al., 2023). Furthermore, burning waste rubber can produce carcinogens and greenhouse gases, aggravating air pollution and climate deterioration (Sienkiewicz et al., 2017). Consequently, it is of significance for sustainability to recycle and effectively utilize waste rubber. Many studies have reported crumb rubber concrete (CRC), in which rubber particles replace fine aggregates for engineering structures. This approach reutilizes waste rubber and simultaneously alleviates the consumption of river sand (Velegrakis et al., 2010; Raffoul et al., 2016; Guo et al., 2022).

Research shows that the ductility, wear resistance, and impact toughness of concrete can be improved after incorporating rubber particles, which contribute to the macroscopic static and seismic behavior of structural concrete (Abendeh et al., 2016; Pham et al., 2020; Karunarathna et al., 2022). Therefore, CRC grants structural energy dissipation properties and

✉ Fangduo XIAO, 12412091@zju.edu.cn
Dongming YAN, dmyan@zju.edu.cn
Fangduo XIAO, https://orcid.org/0009-0004-4959-1208

Received Dec. 27, 2025; Revision accepted May 8, 2026;
Crosschecked June 8, 2026; Online first July 1, 2026

© Zhejiang University Press 2026

enhanced deformation control, which has been increasingly applied in various large-scale infrastructure projects (Liu et al., 2025). Nevertheless, the hydrophobicity of rubber microscopically induces a highly porous interfacial transition zone (ITZ), while its low elastic modulus creates compressible voids, causing severe stress concentrations (Turatsinze and Garros, 2008; Gesoglu et al., 2015). Macroscopically, these defects accelerate microcrack initiation and coalescence under loading, fundamentally undermining the compressive strength (Yan et al., 2025; Mishra et al., 2026; Tan et al., 2026). This reduction, in turn, leads to a pronounced deterioration in the bond strength between the rebar and the CRC matrix (Xiao et al., 2026). The pull-out tests of Gesoglu et al. (2015) on CRC with a maximum rubber replacement ratio (ρ_{rv}) of 30% indicate that the bond strength decreases up to 40% compared with that of normal concrete (NC). Similarly, Bompa and Elghazouli (2017) conducted bond tests of CRC with ρ_{rv} ranging from 0% to 60% in 20% increments and noted that the bond strength gradually decreases with increasing ρ_{rv}. An analogous observation is obtained by Bai et al. (2023).

To compensate for the detrimental effect of rubber incorporation on bond strength, providing additional confinement has emerged as a promising approach. As indicated by the mechanics-based model of Xu et al. (2023), concrete dilation induced by rebar debonding activates passive confinement from external jackets or internal stirrups, generating additional radial stress at the bond interface to enhance bond performance. Traditionally, transverse reinforcement has been widely utilized to provide such well-confined conditions, with bond strength increasing significantly alongside the stirrup ratio (fib, 2013; Wang et al., 2020; Xiao et al., 2025a). Nevertheless, densely arranged internal stirrups can hinder concrete casting and fail to prevent visible surface cracks (Wang et al., 2024). Consequently, externally strengthening members with fiber-reinforced polymer (FRP) sheets to form an FRP–stirrup dual confinement system has become an attractive alternative. In practical engineering scenarios, this strengthening method is highly promising for the seismic retrofitting of bridge piers and the upgrading of existing structural columns, where the superior energy dissipation of CRC and the high tensile strength of FRP can be synergistically utilized. As stated by Wang et al. (2023), specimens under FRP–stirrup dual confinement exhibit bond strengths at least 33.17% and 6.39% higher than unstrengthened and single-stirrup-strengthened specimens, respectively, while also displaying superior bond ductility. Despite these advantages, a critical confinement effect exists, leading to an upper bound for bond strength enhancement (Wang et al., 2024; Xiao et al., 2025a). Once crack development is fully restrained by confinement, further restraining efforts become superfluous and yield no additional bond capacity (Gambarova and Rosati, 1997; Wang et al., 2024). Given the inherently superior crack resistance and toughness of CRC, it is hypothesized that a reduced critical confinement level is required to reach this upper bound. Therefore, further clarification is urgently needed regarding the bond behavior between rebars and CRC under complex confinement conditions, specifically concerning the interplay between ρ_{rv} and the critical confinement threshold. As corresponding studies remain limited, addressing these issues is of vital importance for the reliable and economical design of CRC structures.

To gain insight into this issue, bond tests of rebars to CRC were conducted. The ρ_{rv} ranged from 0% to 40% in 10% increments. With respect to confinement, the specimens included unstrengthened, stirrup-strengthened, FRP-strengthened, and FRP–stirrup dual-strengthened cases. The program was designed to investigate the influence of these variables on the failure mode, bond–slip response, and bond strength. To predict bond strength under different confinement conditions, an analytical model was developed based on elastic–plastic mechanics, which offers better generalization than purely empirical closed-form formulas. Parameters influenced by the ρ_{rv} and confinement conditions were calibrated against test data, enabling more accurate design predictions for the interfacial bond strength of CRC members. Furthermore, a new bond–slip model was proposed to facilitate finite-element simulation of the interfacial bond capacity between steel bars and CRC. Compared with fib (2013), the proposed model achieves better agreement with measured bond–slip responses.

2 Experimental program

2.1 Specimen design

A total of 42 central pull-out specimens were tested. The influential factors considered in the program

included the ρ_{rv}, stirrup confinement, FRP confinement, and FRP–stirrup dual confinement. For the reliability of the test results, two duplicates were prepared for each specimen design. Inspired by the new structural configuration illustrated in Fig. 1, a 16 mm-diameter deformed rebar was embedded along the central axis of a concrete cylinder. Its two ends were wrapped with polyvinyl chloride pipes to avoid stress concentration, resulting in a bonded length of 80 mm, as recommended by CEN (2005). To avert potential cracks induced by thermal effects associated with excessive concrete cover, the ratio of concrete cover to rebar diameter was designed as 2.94, consistent with practical construction details (Tang et al., 2015). In addition, a 6 mm-diameter plain rebar was fabricated into a spiral with a spacing of 40 or 80 mm to serve as internal confinement for selected specimens.

To ensure uniform dispersion of the rubber particles, a forced-action mixer was utilized to dry mix the aggregates and crumb rubber for 2 min to break up any potential clusters, followed by an additional 3 min of wet mixing after introducing cement and water. Concrete was poured vertically into molds. The load-end surface was polished using an angle grinder to ensure smoothness and close contact with the reaction frame during loading. After curing for 28 d, selected specimens were wrapped with one or two layers of FRP sheets, with a 115 mm overlap length to prevent jacket debonding.

Table S1 of the electronic supplementary materials (ESM) lists the specimen parameters and test results in detail. Specimens were named according to the following principles: the first number represents ρ_{rv}; S2 or S3 denotes stirrup spacing of 80 or 40 mm, respectively; F1 or F2 indicates one or two layers of FRP sheets. For instance, 30-S2-F2 denotes a CRC specimen with ρ_{rv} of 30%, strengthened by 80 mm-spacing stirrups and two-layer FRP sheets.

2.2 Material properties

The 42.5-grade ordinary Portland cement was used for all mix proportions. As per ASTM (2018), well-graded aggregates with nominal sizes ranging from 5 to 20 mm were adopted. In accordance with AQSIQ and SAC (2011), river sand with a maximum nominal size of 5 mm, fineness modulus of 2.6, and density of 2650 kg/m^3, respectively, was adopted for fine aggregates. In CRC mixtures, a portion of sand was replaced by rubber particles at volume ratios of 10%, 20%, 30%, and 40%. This specific range was selected to capture the transition of bond behavior while avoiding the excessive mechanical degradation typically observed beyond a 40% replacement. The rubber particle size ranged from 0.25 to 4.00 mm, which matches the gradation of the replaced sand to minimize strength loss, with a density of 925 kg/m^3, consistent with the relevant literature (Bompa and Elghazouli, 2017; Romanazzi et al., 2021; Lu et al., 2024). The mix proportions of the concrete are summarized in Table 1. The four types of rubber: A, B, C, and D, respectively represent their particle sizes of 0.250, 0.425, 1–2, and 2–4 mm. The rubber particle gradation ratios of rubber A, B, C, and D, were designed as 2.25:5.62:10.11:4.49 to achieve a distribution similar to that of the sand, as shown in Fig. 2 (BSI, 1992). For each mix proportion, three duplicate 100 mm cubes were

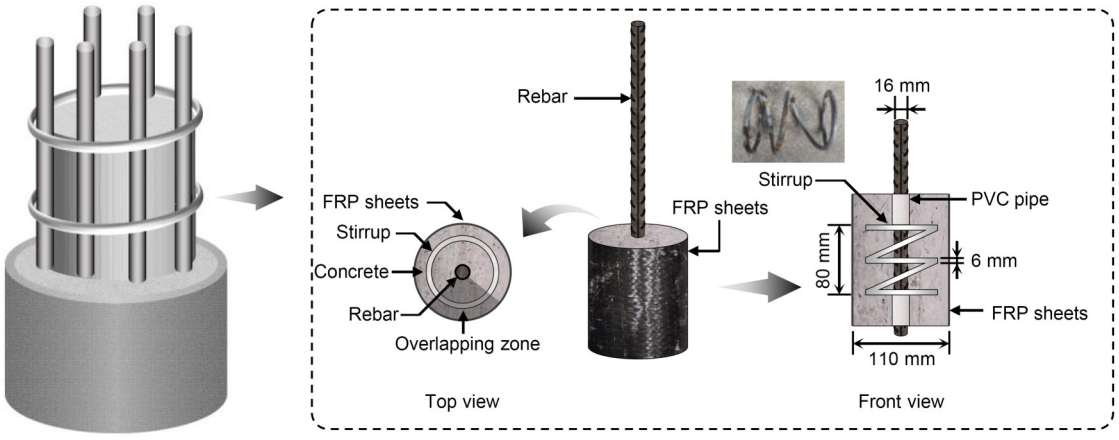


Fig. 1 Schematic of the specimen

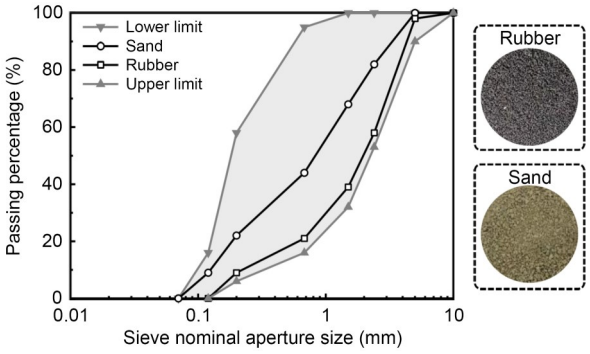


Fig. 2 Particle size distributions of fine aggregates

prepared to determine the compressive strength (f_{cu}), as shown in Fig. 3. It is evident that f_{cu} decreases with increasing ρ_{rv}, which is consistent with the observation of Liu et al. (2023).

A deformed rebar with a nominal diameter (d) of 16 mm was used, and the corresponding surface geometry was measured using a Vernier caliper, as shown in Fig. 4. In accordance with AQSIQ and SAC (2010), the tensile stress–strain curves of the three duplicate rebars (rebars 1–3) were obtained.

As per the manufacturer's information, the FRP parameters were listed in Table 2. Additionally, the interfacial bond strength between the concrete and FRP sheets was 5.4 MPa in accordance with MOHURD and AQSIQ (2011).

2.3 Test setup

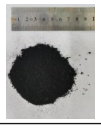
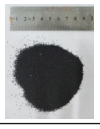
The central pull-out tests were conducted via a 200 kN servo-controlled test machine. As per Xiao et al. (2025b), the displacement-controlled rate was 1 mm/min. As illustrated in Fig. 5, the load-end surface of the concrete was in close contact with the homemade frame, while the load-end reinforcement was clamped by a chuck. The applied force was measured by a load cell. A pair of linear variable displacement transducers (LVDTs) fixed on the steel frame served to capture the load-end slip, and an LVDT fixed on the magnetic base was used to collect the free-end slip.

3 Test results

3.1 Bond–slip response and failure mode

As recommended by RILEM (1994), the embedment length of 5d allows approximately uniform stress

Table 1 Mix proportions of concrete

	Mix proportions of concrete (kg/m^3)								
	Cement	Fly ash	Dravel	Sand	Rubber A	Rubber B	Rubber C	Rubber D	Water
ρ_{rv}									
0%	373	50	1273	637	0.00	0.00	0.00	0.00	170
10%	373	50	1273	573	2.25	5.62	10.11	4.49	170
20%	373	50	1273	510	4.49	11.24	20.23	8.99	170
30%	373	50	1273	446	6.74	16.85	30.34	13.48	170
40%	373	50	1273	382	8.99	22.47	40.45	17.98	170

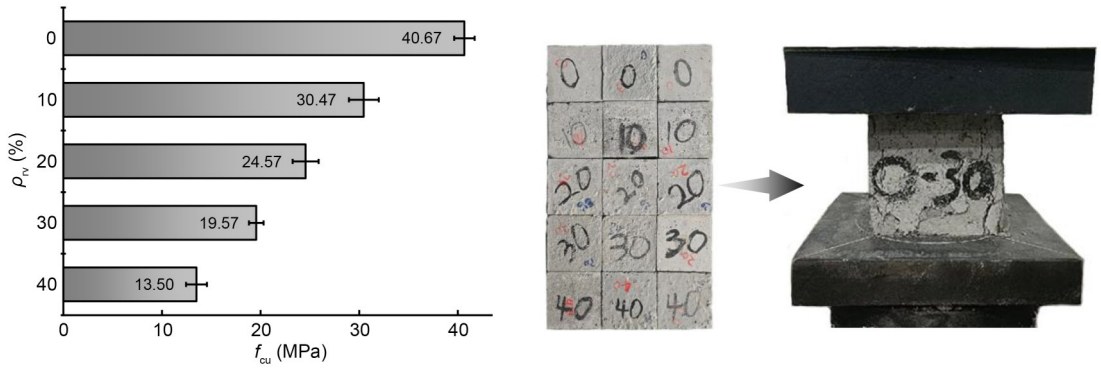


Fig. 3 Test results of concrete strength

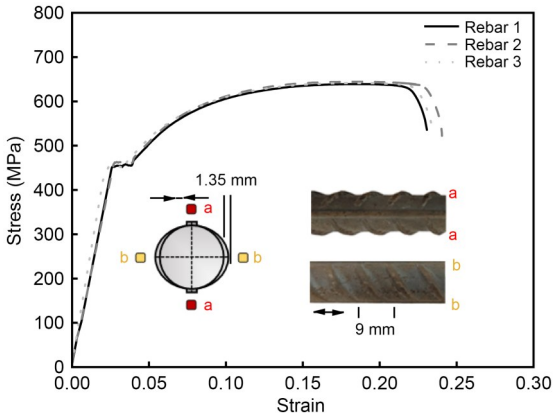


Fig. 4 Stress–strain curves and surface geometry of the reinforcement. a–a and b–b stand for the different observation perspectives

Table 2 Parameters of FRP sheets

Parameter	Value
Areal weight (g/m^2)	299
Nominal thickness (mm)	0.167
Tensile strength (MPa)	3739
Elastic modulus (GPa)	240
Ultimate rupture strain	0.0171

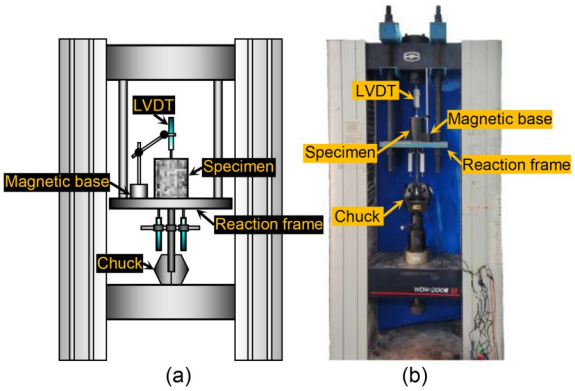


Fig. 5 Test setup: (a) schematic; (b) photograph

along the bonded zone. Thus, Eq. (1) was used to determine the bond stress (τ). Considering rebar deformation between the load-end LVDTs and the bonded region, Eq. (2) was adopted to determine nominal slip (s) (Xiao et al., 2025b).

$$\tau = \frac{F}{\pi d l}, \tag{1}$$

$$s = \frac{1}{2}\left(s_1 + s_f - \frac{4Fl_a}{\pi d^2 E_s}\right), \tag{2}$$

where F is the pull-out load; l is the embedment length; s_1 is the load-end slip; s_f is the free-end slip; l_a is the distance between the load-end LVDTs and bonded region; E_s is the reinforcement elastic modulus.

Fig. 6 illustrates the bond–slip curves of the unstrengthened specimens, most of which exhibit only the pre-peak branch due to splitting failure. In this case, circumferential stress exceeds the tensile capacity of concrete and induces multiple cracks, resulting in loss of confinement to the core concrete. Therefore, a post-peak branch cannot develop under splitting failure, consistent with the bond–slip response under insufficient confinement reported in fib (2013). Moreover, ρ_{rv} plays an important role in the bond–slip behavior of unstrengthened specimens: the initial bond stiffness decreases as ρ_{rv} increases. Wang et al. (2020) reported that the initial bond–slip behavior is governed by chemical adhesion. However, incorporating rubber particles reduces the area of cement paste in contact with the steel surface, indirectly weakening the chemical adhesion.

Additionally, the macroscopic failure is significantly influenced by ρ_{rv}. For NC specimens (ρ_{rv}=0%), pronounced brittleness is evidenced by more than three visible cracks on the free-end surface. With increasing

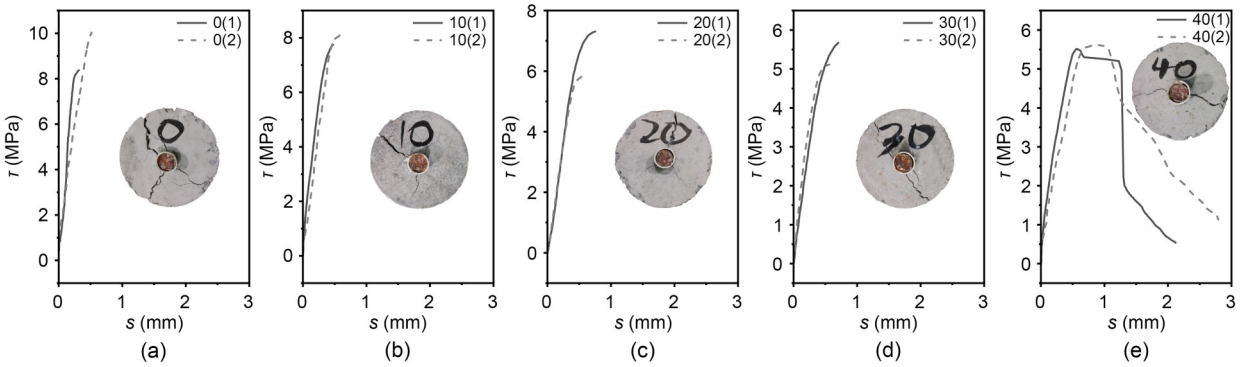


Fig. 6 Bond–slip curves and failure phenomena of unstrengthened specimens with different ρ_{rv} values: (a) ρ_{rv}=0%; (b) ρ_{rv}=10%; (c) ρ_{rv}=20%; (d) ρ_{rv}=30%; (e) ρ_{rv}=40%. (1) and (2) represent two parallel experiments of a single specimen

ρ_{rv}, cracking is alleviated. Specifically, for ρ_{rv}=10% and 20%, three cracks remained visible, but their widths were significantly smaller than those in NC specimens. When ρ_{rv} increased to 30%, only two visible cracks propagated to the concrete cover edge, although splitting failure still occurred. When ρ_{rv} further increased to 40%, the failure mode changed into pull-out failure with splitting. In this case, the concrete matrix still provides weak confinement to the bond interface, and a ductile post-peak segment can be observed. This is because crack tips are blunted by rubber particles, restraining crack propagation (Bai et al., 2023).

All specimens strengthened by confinement components underwent pull-out failure, and typical ductile bond–slip curves were obtained (Fig. 7), featuring a post-peak branch with soft unloading stiffness. This indicates that crack-induced concrete dilation activates the mechanical response of stirrups or FRP, which in turn provides confinement to the core region and contributes to ductile bond–slip behavior. However, the unloading stiffness of CRC specimens is smaller than that of NC specimens under identical confinement conditions. This may be attributed to the porous structure of CRC arising from the weak rubber–matrix interface, which allows greater energy dissipation (Ganjian et al., 2009; Hall and Najim, 2014).

Note that a certain degree of variability exists between the duplicate specimens. This is attributed to the inherent heterogeneity of the concrete matrix. The random spatial distribution of aggregates near the rebar ribs leads to localized variations in the mechanical interlocking force. Furthermore, the highly sensitive nature of the concrete failure mechanism inherently contributes to the observed scatter in bond strength.

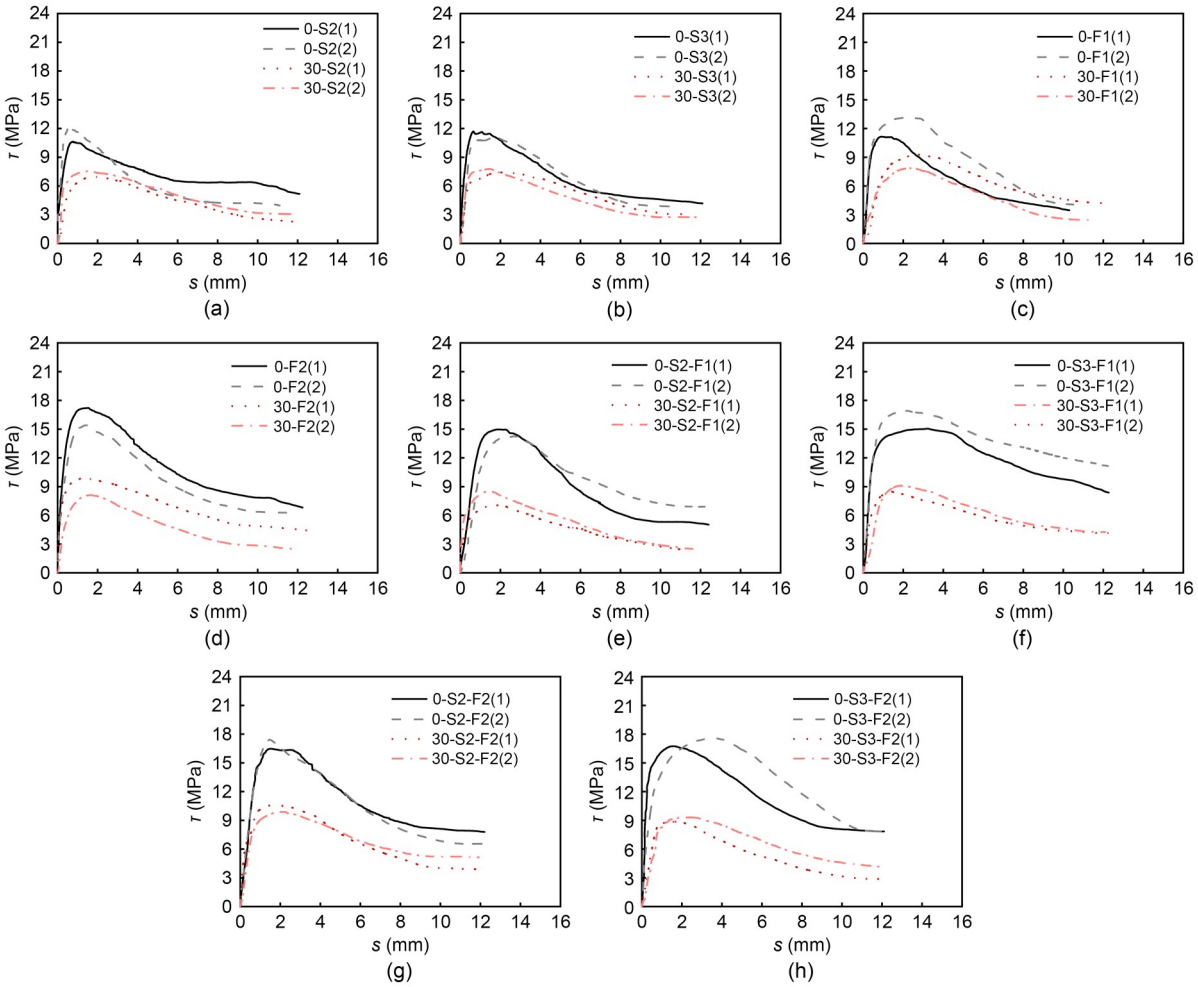


Fig. 7 Bond–slip curves of strengthened specimens: (a) *x*-S2; (b) *x*-S3; (c) *x*-F1; (d) *x*-F2; (e) *x*-S2-F1; (f) *x*-S3-F1; (g) *x*-S2-F2; (h) *x*-S3-F2. *x* is 0 or 30. (1) and (2) represent two parallel experiments of a single specimen

3.2 Factors influencing bond strength

3.2.1 Impact of rubber replacement ratio

Fig. 8 shows the influence of ρ_{rv} on the ultimate bond strength (τ_u) of the unstrengthened specimens. The bond strength decreases as ρ_{rv} increases from 0% to 30%, which is expected due to the reduction in f_{cu}. Notably, the bond strength of specimen 40 is higher than that of specimen 30, although its f_{cu} is only 68.98% of the latter. This can be attributed to the different failure modes. For specimen 40, which underwent pull-out failure with splitting, the partially intact concrete matrix enables continued interaction between rebar and concrete, leading to more fully developed bond stress than in splitting failure. This finding suggests that a critical ρ_{rv} may result in a balance between bond strength and ductility for the anchorage design of CRC members.

As recommended by fib (2013), the interfacial bond strength can be normalized to exclude the influence of compressive strength using the bond coefficient $\gamma_b=\tau_u/(f_{cu})^{0.5}$. Fig. 8 shows that γ_b gradually decreases as ρ_{rv} increases from 0% to 30%, indicating that the normalized bond capacities of CRC specimens are lower than that of NC specimen. This reduction may be associated with changes in tensile strength that alter crack inclination in front of steel bars and reduce the concrete-bar wedge effect. Alternatively, rubber particles with a low elastic modulus and high Poisson's ratio may modify frictional behavior at the rebar–CRC interface (Topçu, 1995; Bompa and Elghazouli, 2017).

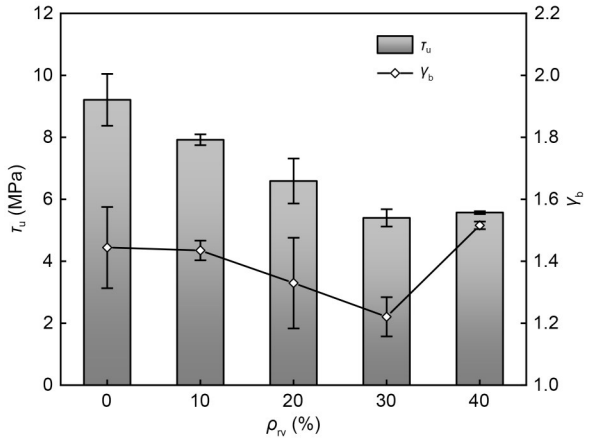


Fig. 8 Influence of ρ_{rv} on τ_u of the unstrengthened specimens

3.2.2 Impact of additional confinement

Fig. 9 shows the influence of confinement conditions on bond strength. As shown in Fig. 9a, confinement significantly increases the bond strength. For example, the bond strength of strengthened NC and CRC specimens is 23.24% and 34.07% higher than that of their unstrengthened counterparts, respectively. The effect of stirrups/FRP can be attributed to increased radial pressure at the bond interface and restrained cracking, which ensures sustained interaction between rebar and surrounding concrete (Xu et al., 2023; Xiao et al., 2025a). FRP generally outperforms stirrups because it confines a larger region (Xu et al., 2023), and a similar conclusion is found by Wang et al. (2023).

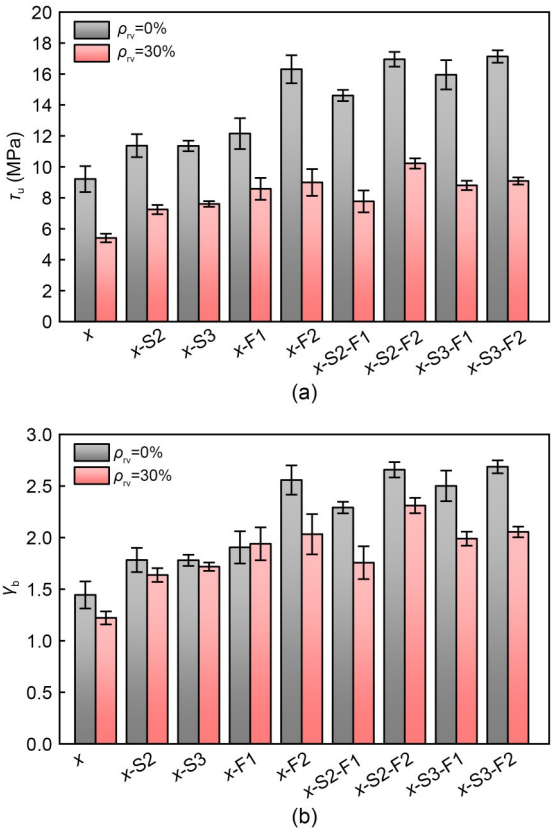


Fig. 9 Influence of different confinement conditions on (a) bond strength and (b) bond coefficient. *x* is 0 or 30

In addition, it is found that reducing stirrup spacing plays a negligible role in bond strength. For instance, the bond strength of specimen 30-S3 is merely 4.97% higher than that of specimen 30-S2, and the bond strength between specimens 0-S3 and 0-S2 nearly coincides. In contrast, the increase in the number of

FRP layers heavily improves the bond strength of the NC specimens, as the bond strength of specimen 0-F2 is 34.24% higher than that of its one-layer FRP-strengthened counterpart (0-F1). Interestingly, the bond strength of the CRC specimen confined by two layers of FRP is only 4.78% higher than that of specimen 30-F1. This may be attributed to the deviation in fracture energy between the two types of concrete. The superior crack resistance of CRC induces additional FRP confinement redundancy. Similar phenomena are also observed for specimens strengthened by dual confinement. It is apparent that the bond strength of NC specimens is enhanced by improving the confinement level. For example, in terms of the specimens with 40 mm-spacing stirrups, the bond strength is 11.35, 15.95, and 17.13 MPa when the number of layers of FRP sheets is 0, 1, and 2. Alternatively, for specimens wrapped with single-layer FRP, the bond strength ratios of specimens 0-S2-F1 and 0-S3-F1 to 0-F1 are 1.20 and 1.31, respectively. However, the bond strength varies little for CRC specimens under different confinement levels. It can be inferred that the bond strength of well-confined CRC members is heavily dominated by the interfacial characteristics rather than the additional confinement. This finding indicates that the mix proportion of CRC should be emphasized in anchorage design, enabling potential savings in confinement cost.

Fig. 9b compares CRC and NC specimens using γ_b. The majority of test results show that the γ_b of NC specimens remains superior to that of CRC specimens regardless of confinement conditions. Therefore, an additional safety coefficient is required in CRC structural design, even when confinement is provided, considering the strength degradation caused by rubber incorporation.

4 Analytical bond strength model

4.1 Performance evaluation of existing models

In accordance with the following criteria, a database was assembled from relevant studies (Choi et al., 2014; Gao et al., 2019; Li et al., 2020; Kammash et al., 2022; Bai et al., 2023): (a) only specimens cast with NC or CRC were covered, and other types of concrete, e.g., seawater sea–sand concrete, geopolymer concrete, and fiber-reinforced concrete, were excluded; (b) only the bond behavior of deformed carbon steel bars was compared; (c) with respect to the strengthened specimens, only the device of stirrups or FRP was considered. Table S2 of the ESM lists more details of the database. By comparing the experimental data to the theoretical predictions of fib (2013), the notable nonconservative predictions for the CRC specimens are inspected from Fig. 10a. Consequently, fib (2013) may be inadequate for the anchorage design of CRC structures due to differences in interfacial mechanisms. In this case, several novel models were developed by directly fitting the bond test results of CRC specimens, e.g., Li et al. (2024) and Chen et al. (2023). However, these closed-form formulas cannot take comprehensive factors into consideration, leading to poor generalization (Figs. 10b and 10c), as reflected by undesirable statistical indicators, i.e., mean absolute error (E_{MA}), root mean squared error (E_{RMS}), mean (M), and coefficient of variation (C_V). This may be caused by the fact that such empirical models are developed based on the variables designed in the experiment, whereas the factors outside of the predesign cannot be captured. Therefore, analytical modeling for the interfacial bond strength between rebar and CRC based on physical assumptions is needed due to its excellent extrapolation for the scenarios outside of the source database (Zhang et al., 2019; Xu and Yan, 2023; Xu et al., 2023).

4.2 Mechanics-based model

4.2.1 Radial stress

As shown in Fig. 11, the fictitious crack assumption defines a double-cylinder model consisting of an inner plastic region and outer elastic region (Li et al., 2021), where r_s, r_{cr}, and r_c are the rebar radius, fictitious crack radius, and specimen radius, respectively. The fictitious crack model sets the tangential stress at the crack tips equal to the concrete tensile strength (f_t), resulting in constant concrete strain (ε_{cr}) within the plastic region. According to the equilibrium of deformation, the crack width (w_c) evolves linearly along the radial direction and is expressed by Eq. (3) (Xu and Yan, 2023; Xu et al., 2023).

$$w_c = \frac{2\pi\varepsilon_{cr}}{N}(r_{cr}-r) = \frac{2\pi f_t}{NE_c}(r_{cr}-r), \tag{3}$$

where N is the crack number; r is the arbitrary radial coordinate; E_c is the elastic modulus of concrete.

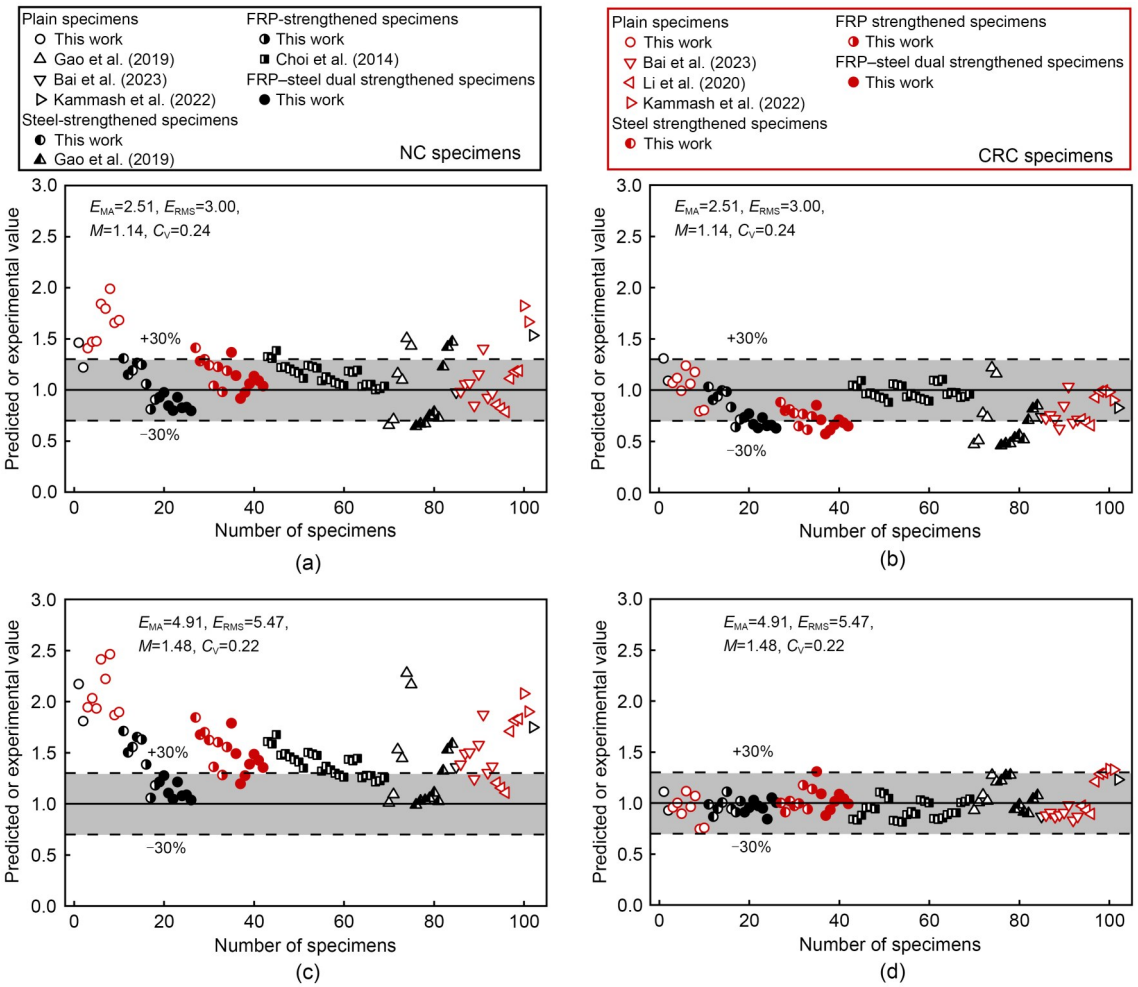


Fig. 10 Prediction accuracy of bond strength models: (a) model of fib (2013); (b) model of Li et al. (2024); (c) model of Chen et al. (2023); (d) proposed model in this work

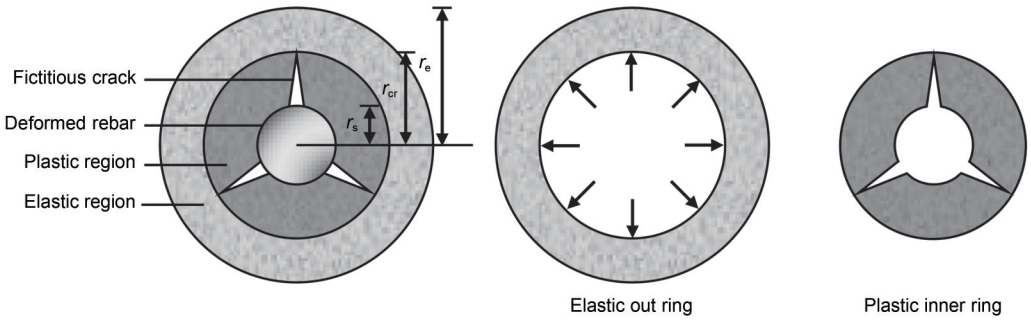


Fig. 11 Fictitious crack model

The cohesion ($\sigma_{w,r}$) within cracks provides bridging traction, which governs the radial stress on the bond interface from the inner plastic region. In this sense, a corresponding analytical solution is obtained using the exponential constitutive $\sigma_{w,r}$–w_c model reported by Reinhardt et al. (1986). On the other hand, the interfacial radial stress from the outer elastic region is equilibrated with the uniform pressure at the inner wall of the elastic cylinder, which is inspired by the hydraulic pressure analogy. Thus, the radial stress (σ_1) provided by the concrete cover can be calculated by Eq. (4).

$$\sigma_1 = f_t \frac{r_{cr}}{r_s} \frac{r_e^2 - r_{cr}^2}{r_e^2 + r_{cr}^2} + \frac{\int_{r_s}^{r_{cr}} \sigma_{w,r}\, dr}{r_s}. \tag{4}$$

The contribution of stirrups/FRP arises because crack-induced dilation causes tensile deformation in these components, activating confinement and increasing radial stress at the bond interface. The radial stress (σ_2) provided by stirrups/FRP is expressed by Eq. (5), where the strain of the confinement component is determined by Eqs. (6) and (7) for the cases without and with crack penetration at the component location, respectively.

$$\sigma_2 = \frac{E_{st}\varepsilon_{st}A_{st}}{2r_s l} + \frac{E_f\varepsilon_f A_f}{2r_s l}, \tag{5}$$

$$\begin{cases} \varepsilon_{st} = \varepsilon_{cr} \dfrac{r_e^2 + r_{st}^2}{r_e^2 + r_{cr}^2} \dfrac{r_{cr}^2}{r_{st}^2}, \\ \varepsilon_f = \varepsilon_{cr} \dfrac{2r_{cr}^2}{r_e^2 + r_{cr}^2}, \end{cases} \tag{6}$$

$$\begin{cases} \varepsilon_{st} = \dfrac{Nw_{st} + 2\pi r_{st}\varepsilon_{cr}}{2\pi r_{st}}, \\ \varepsilon_f = \dfrac{Nw_f + 2\pi r_e\varepsilon_{cr}}{2\pi r_e}, \end{cases} \tag{7}$$

where E_{st} and E_f are the elastic moduli of the stirrup and FRP, respectively; A_{st} and A_f are the cross-sectional areas of the stirrup and FRP, respectively; ε_{st} and ε_f are the strains of stirrup and FRP, respectively; r_{st} is the radial coordinate where the stirrup is located; w_{st} and w_f are the crack widths at $r=r_{st}$ and $r=r_e$, respectively.

By increasing r_{cr} with a given step length until the calculated radial stress computed at the current r_{cr} is no larger than that at the previous r_{cr}, the governing radial stress for ultimate bond stress is obtained.

4.2.2 Bond stress

Existing analytical models indicate that the bond stress comprises two components, i.e., the concrete-to-concrete wedge effect and concrete-to-steel friction (Choi and Lee, 2002; Zhang et al., 2019; Xu et al., 2022). The former is associated with crushed concrete with an inclined failure surface ahead of the steel bars. The latter is controlled by the global friction between the steel bar and concrete within a bond unit. In this sense, the bond stress can be obtained by Eq. (8), in which the resultant radial stress is considered the dominant factor.

$$\tau = (\sigma_1 + \sigma_2)\left[\frac{\sin\alpha + \mu_1\cos\alpha}{\cos\alpha - \mu_1\sin\alpha}\frac{2\pi r_s h_r \cot\alpha}{2\pi r_s(s_c + s_r)} + \frac{\mu_2 2\pi r_s s_c + \mu_2(2\pi r_s + 2\pi h_r)s_r}{2\pi r_s(s_c + s_r)}\right], \tag{8}$$

where α is the angle of concrete cone in front of rebar; h_r is the rib height; μ_1 is the concrete-to-concrete friction coefficient; μ_2 is the concrete-to-steel friction coefficient; s_c is the rib spacing between two adjacent ribs; s_r is the rib width.

However, compared with NC specimens, the inferior γ_b as well as the critical effect of confinement should both be carefully considered for the bond strength model of CRC specimens. First, based on regression analysis, a coefficient ξ_r dependent on ρ_{rv} is proposed to capture the impact of rubber on the macroscopic bond strength (Eq. (9)).

$$\xi_r = \exp(-0.342\rho_{rv}). \tag{9}$$

In addition, since the inherent crack resistance of CRC can render additional confinement redundant, the bond strength model is further improved using Eq. (10) by incorporating the critical σ_2.

$$\tau = \begin{cases} (\sigma_1 + \sigma_2)\left[\dfrac{\sin\alpha + \mu_1\cos\alpha}{\cos\alpha - \mu_1\sin\alpha}\dfrac{2\pi r_s h_r \cot\alpha}{2\pi r_s(s_c + s_r)} + \dfrac{\mu_2 2\pi r_s s_c + \mu_2(2\pi r_s + 2\pi h_r)s_r}{2\pi r_s(s_c + s_r)}\right]\xi_r, & \dfrac{\sigma_2}{f_t} \leqslant 3.76, \\ (\sigma_1 + 3.76 f_t)\left[\dfrac{\sin\alpha + \mu_1\cos\alpha}{\cos\alpha - \mu_1\sin\alpha}\dfrac{2\pi r_s h_r \cot\alpha}{2\pi r_s(s_c + s_r)} + \dfrac{\mu_2 2\pi r_s s_c + \mu_2(2\pi r_s + 2\pi h_r)s_r}{2\pi r_s(s_c + s_r)}\right]\xi_r, & \dfrac{\sigma_2}{f_t} > 3.76. \end{cases} \tag{10}$$

Other material parameters within the bond strength model are summarized in Table S3 of the ESM in accordance with existing reports (Reinhardt et al., 1986; AQSIQ and SAC, 2007; fib, 2013; Bompa and Elghazouli, 2017; ASTM, 2018; Ka et al., 2018; Zhao and Zhu, 2018). As illustrated in Fig. 10d, the proposed

model outperforms existing models in terms of prediction accuracy, accompanied by desirable statistical indicators.

5 Continuous bond–slip model

5.1 Theoretical modeling

The macroscopic response induced by rebar debonding, in fact, is the comprehensive manifestation of the stochasticly distributed microscopic damage, covering microcracks, voids, and defects (Huang et al., 2019b). Due to the intrinsic heterogeneity of concrete materials, the bond–slip responses among duplicate specimens still present deviations, as shown in Fig. 12a. To phenomenologically simulate the stochasticity of the bond–slip response, the concrete–rebar bond is described by the behavior of n spring–friction units with duplicate stiffness (K) (Fig. 12b). The assumed spring element follows linear elasticity up to a critical tensile extension (Δ) and services for transmitting the bond stress. However, the bond stress will be transferred to the friction element to bear once the spring element fractures. Thus, the bond–slip response induced by a bond unit is depicted in Fig. 12c, which can be expressed by Eq. (11). By giving different mechanics parameters to each spring element, they will be subjected to stochastic fracture, resulting in the rewritten expression of the bond–slip response determined by a bond unit (Eq. (12)). The fracture of multiple springs results in macroscopic nonlinearity, a significant characteristic of the bond–slip response (Huang et al., 2019b), as illustrated in Fig. 12d where σ and ε stand for the tensile stress and strain of spring elements, respectively.

$$\tau_i=\begin{cases}Ks, & s\leqslant\Delta,\\ \tau_r, & s>\Delta,\end{cases} \tag{11}$$

$$\tau_i=[1-H(s-\Delta)]Ks+H(s-\Delta)\tau_r, \tag{12}$$

where τ_i (i=1, 2, ⋯, n) is the bond stress of the ith bond unit; τ_r is the residual bond stress determined by the friction element; H is the Heaviside function.

As depicted in Eq. (13), the stochastic fracture of the spring system composed of n units can be expressed by a damage variable (D), and hence, the macroscopic bond–slip response is written as Eq. (14).

$$D=\frac{\sum_{i=1}^{n}H(s-\Delta)}{n}, \tag{13}$$

$$\tau=(1-D)Ks+D\tau_r. \tag{14}$$

The reasonable definition of D is of great significance to ensure the continuity of the bond–slip model because the joint selection of the segmented model significantly affects the calculated results of the finite-element capacity and causes inconsistencies near joints, e.g., fib (2013). To address this issue, the Weibull density function ($f(\delta)$) shown in Eq. (15) is adopted due to its suitability for quasibrittle fracture. Accordingly, D is expressed by Eq. (16) and accords with the mandatory constraints, i.e., $0\leqslant D(s)\leqslant 1$, $D(s=0)=0$, and $\mathrm{d}D(s)\geqslant 0$ (Huang et al., 2019a).

$$f(\delta)=\frac{k}{\lambda}\left(\frac{\delta}{\lambda}\right)^{k-1}\exp\left(-\frac{\delta^k}{\lambda^k}\right), \tag{15}$$

$$D=\int_0^s f(\delta)\,\mathrm{d}\delta=\frac{k}{\lambda}\left(\frac{\delta}{\lambda}\right)^{k-1}\exp\left(-\frac{\delta^k}{\lambda^k}\right)\mathrm{d}\delta=1-\exp\left(-\frac{s^k}{\lambda^k}\right), \tag{16}$$

where δ is the stochastic variable for describing spring fracture; k and λ are the shape and scale parameters of the Weibull distribution, respectively (Xiao et al., 2025a).

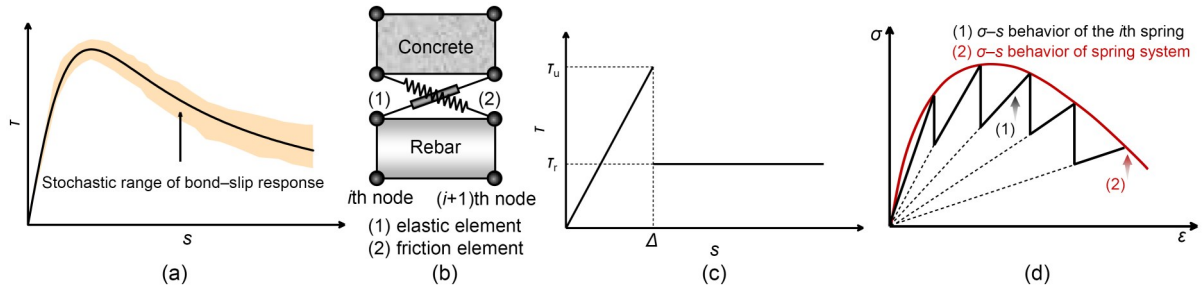


Fig. 12 Manifestation of the stochasticity and nonlinearity of the bond–slip response: (a) stochasticity of bond–slip response; (b) bond unit; (c) stochastic fracture of a spring element; (d) nonlinearity induced by *n* spring elements

5.2 Parameter calibration for the bond–slip model

5.2.1 Residual bond behavior

Zhao and Zhu (2018) defined that the residual behavior is achieved as the slip arrives at $s=s_c+s_r$. In this sense, the ratios (ψ) of residual bond stress (τ_r) to ultimate bond stress (τ_u) are presented in Figs. 13a and 13b for the NC and CRC specimens, which are proposed as 0.48 and 0.46, respectively.

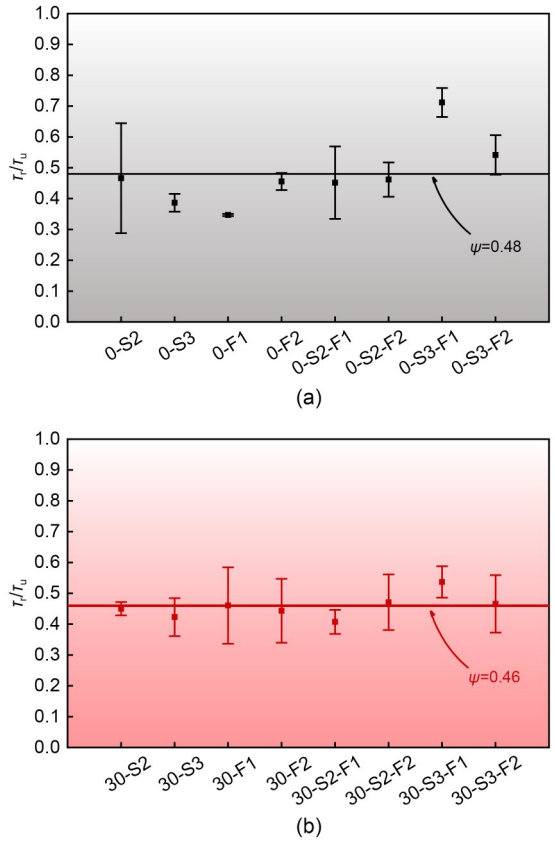


Fig. 13 Calibration of residual bond stress: (a) NC specimens; (b) CRC specimens

5.2.2 Spring stiffness

The spring stiffness K is inherently determined by the material and structural parameters of the specimens, despite the loading conditions. Unfortunately, the assumed parameter K fails to be obtained by means of experiments, and the corresponding analytical determination is absent in existing studies. As a result, the bond strength calculated via the foregoing analytical model will be employed to invert it hereinafter.

As depicted in Eq. (17), the ultimate bond stress can be expressed in another form. In addition, $\delta\tau_u/\delta s_u=0$ is noted near the ultimate state due to the continuity of the proposed bond–slip model. By inputting this condition into Eq. (17), the value of K can be easily determined.

$$\tau_u=\exp\left(-\frac{s_u^k}{\lambda^k}\right)Ks_u+\left[1-\exp\left(-\frac{s_u^k}{\lambda^k}\right)\right]\psi\tau_u, \quad (17)$$

where s_u is the slip under τ_u.

5.3 Model validation

Fig. 14 shows the comparisons of the experimental bond–slip curves to the theoretical predictions of the proposed model as well as the model of fib (2013), while the integral absolute error (E_{IA}) is used to quantify the accuracy. In contrast, the proposed model achieves superior agreement with the stochastic range of the bond–slip response, and the corresponding E_{IA} for all cases is less than 20%. Although an anomalous phenomenon is inspected in Fig. 14i, the accuracy of the proposed model, i.e., E_{IA}=10.47%, is still acceptable.

To facilitate practical engineering applications, the proposed continuous bond–slip model can be incorporated into finite element analysis. This integration enables the accurate simulation of the nonlinear macroscopic behavior and the superior energy dissipation of confined members, thereby providing a reliable numerical tool for the seismic design of CRC structures.

6 Conclusions

This novel evolution law of bond behavior revealed in the present study differed from those of previous research because the coupling effect of the ρ_{rv} and additional confinement was comprehensively discussed. The following conclusions are meaningful for the structural design of sustainable engineering:

(1) The increase in ρ_{rv} significantly degrades the bond strength of unstrengthened specimens but contributes to the postponement of the development of concrete cracks. As ρ_{rv} increases to 40%, the brittle splitting failure of unstrengthened specimens tends to transform into pull-out failure with splitting, while the bond strength degradation is conspicuously alleviated, which inspires a potential ρ_{rv} to synchronously achieve

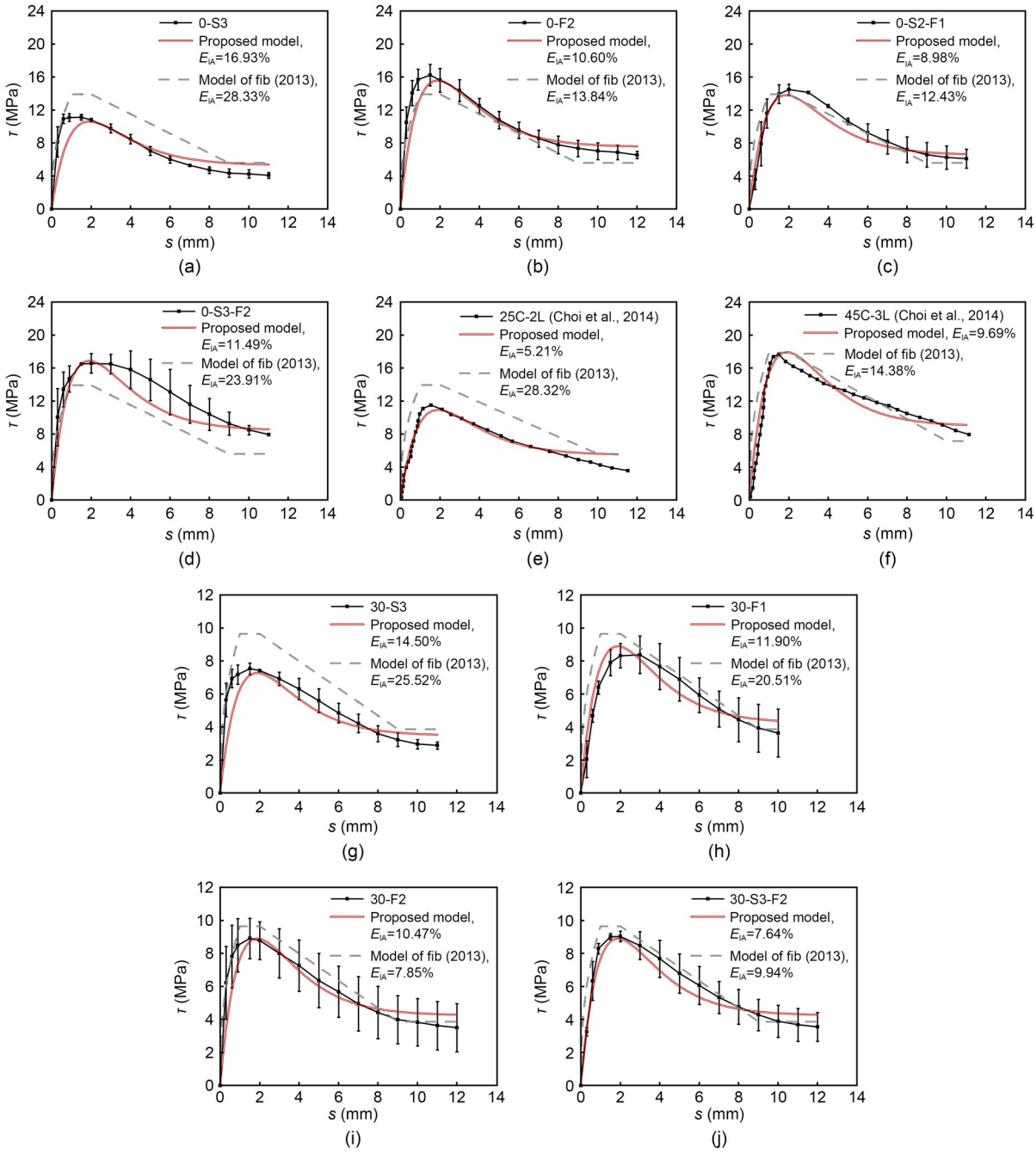


Fig. 14 Comparisons of theoretical predictions to experimental results: (a) 0-S3; (b) 0-F2; (c) 0-S2-F1; (d) 0-S3-F2; (e) 25C-2L; (f) 45C-3L; (g) 30-S3; (h) 30-F1; (i) 30-F2; (j) 30-S3-F2

the optimal bond strength and ductility for CRC member design.

(2) Compared with the unstrengthened specimens, the use of stirrup/FRP confinement is apparent to improve the bond behavior regardless of the concrete type. Nevertheless, the increase in confinement level contributes to the bond strength of NC specimens but plays a negligible role in that of CRC specimens. This finding proposes that the usage of confinement devices should be considered for the anchorage design of CRC members.

(3) An analytical model based on fictitious crack theory is proposed for predicting the bond strength of steel rebars to CRC, which is further improved by taking the degradation coefficient (ξ_τ) and the critical confinement effect into consideration. The composite

spring–friction system is assumed to establish a continuous bond–slip model. The high predicted accuracy, as well as the stochasticity and nonlinearity of the bond–slip response, is synchronously revealed.

Nevertheless, the evolution law of bond behavior revealed in this study is only accepted for quasistatic conditions, failing to reflect the transient responses of earthquake-stricken structures. Furthermore, investigating the coupling effects of steel corrosion and external confinement on the bond degradation mechanisms of CRC members is needed. Finally, the proposed degradation coefficient (ξ_r) in the present form cannot manifest the threshold effect of the ρ_{rv}, which should be determined based on further bond tests.

Acknowledgments

This work is supported by the Zhejiang Provincial Natural Science Foundation of China (No. LTGG23E080008). We thank Chenkang LI and Weiqi SUN (State Key Laboratory of Coastal and Offshore Engineering, Dalian University of Technology, China) for their generous assistance in the experimental work.

Author contributions

Qiang LI designed the research. Fangduo XIAO wrote the first draft of the manuscript. Shiwei LU and Jizhong WANG processed the corresponding data. Shikun CHEN helped to organize the manuscript. Dongming YAN revised and edited the final version.

Conflict of interest

Dongming YAN is an Editorial Board member of this journal, and is NOT involved in the editorial review or the decision to publish this article. Qiang LI, Fangduo XIAO, Shiwei LU, Jizhong WANG, Shikun CHEN, and Dongming YAN declare that they have no conflicts of interest.

Declaration on the use of generative AI tools

No generative AI tools were used in the preparation of this manuscript.

Data availability

The data that support the findings of this study are available from the corresponding author upon reasonable request.

References

Abendeh R, Ahmad HS, Hunaiti YM, 2016. Experimental studies on the behavior of concrete-filled steel tubes incorporating crumb rubber. *Journal of Constructional Steel Research*, 122:251-260. https://doi.org/10.1016/j.jcsr.2016.03.022

AQSIQ (General Administration of Quality Supervision, Inspection and Quarantine of the People's Republic of China), SAC (Standardization Administration of the People's Republic of China), 2007. Steel for the Reinforcement of Concrete-Part 2: Hot Rolled Ribbed Bars, GB 1499.2-2007. National Standards of the People's Republic of China (in Chinese).

AQSIQ (General Administration of Quality Supervision, Inspection and Quarantine of the People's Republic of China), SAC (Standardization Administration of the People's Republic of China), 2010. Metallic Materials-Tensile Testing-Part 1: Method of Test at Room Temperature, GB/T 228.1-2010. National Standards of the People's Republic of China (in Chinese).

AQSIQ (General Administration of Quality Supervision, Inspection and Quarantine of the People's Republic of China), SAC (Standardization Administration of the People's Republic of China), 2011. Sand for Construction, GB/T 14684-2011. National Standards of the People's Republic of China (in Chinese).

ASTM (Advancing Standards Transforming Markets), 2018. Standard Specification for Concrete Aggregates, ASTM C33/C33M-18. ASTM International, West Conshohocken, USA.

Azevedo F, Pacheco-Torgal F, Jesus C, et al., 2012. Properties and durability of HPC with tyre rubber wastes. *Construction and Building Materials*, 34:186-191. https://doi.org/10.1016/j.conbuildmat.2012.02.062

Bai YH, Zhang DY, Chen K, et al., 2023. Experimental study and numerical simulation on the bonding properties of rubber concrete and deformed steel bar. *Construction and Building Materials*, 383:131416. https://doi.org/10.1016/j.conbuildmat.2023.131416

Bompa DV, Elghazouli AY, 2017. Bond-slip response of deformed bars in rubberised concrete. *Construction and Building Materials*, 154:884-898. https://doi.org/10.1016/j.conbuildmat.2017.08.016

BSI (British Standards Institution), 1992. Specification for Aggregates from Natural Sources for Concrete, BS 882:1992. BSI, London, UK.

CEN (European Committee for Standardization), 2005. Steel for the Reinforcement of Concrete-Weldable Reinforcing Steel-General, EN 10080:2005. CEN, Brussels, Belgium.

Chen YX, Zhao YF, Zeng L, et al., 2023. Bond performance and bond-slip constitutive model for rebar embedded in rubber powder-modified polypropylene fiber reinforced concrete. *Construction and Building Materials*, 375:130934. https://doi.org/10.1016/j.conbuildmat.2023.130934

Choi E, Cho BS, Jeon JS, et al., 2014. Bond behavior of steel deformed bars embedded in concrete confined by FRP wire jackets. *Construction and Building Materials*, 68:716-725. https://doi.org/10.1016/j.conbuildmat.2014.06.092

Choi OC, Lee WS, 2002. Interfacial bond analysis of deformed bars to concrete. *Structural Journal*, 99(6):750-756. https://doi.org/10.14359/12339

Ferdous W, Manalo A, Siddique R, et al., 2021. Recycling of landfill wastes (tyres, plastics and glass) in construction-a review on global waste generation, performance, application and future opportunities. *Resources, Conservation and Recycling*, 173:105745. https://doi.org/10.1016/j.resconrec.2021.105745

fib, 2013. fib Model Code for Concrete Structures 2010. Ernst & Sohn, Berlin, Germany.

Gambarova PG, Rosati GP, 1997. Bond and splitting in bar pull-out: behavioural laws and concrete cover role. *Magazine of Concrete Research*, 49(179):99-110. https://doi.org/10.1680/macr.1997.49.179.99

Ganjian E, Khorami M, Maghsoudi AA, 2009. Scrap-tyre-rubber replacement for aggregate and filler in concrete. *Construction and Building Materials*, 23(5):1828-1836. https://doi.org/10.1016/j.conbuildmat.2008.09.020

Gao K, Li Z, Zhang JR, et al., 2019. Experimental research on bond behavior between GFRP bars and stirrups-confined concrete. *Applied Sciences*, 9(7):1340. https://doi.org/10.3390/app9071340

Gesoglu M, Güneyisi E, Hansu O, et al., 2015. Influence of waste rubber utilization on the fracture and steel–concrete bond strength properties of concrete. *Construction and Building Materials*, 101:1113-1121. https://doi.org/10.1016/j.conbuildmat.2015.10.030

Guo Q, Wang S, Zhang RY, 2022. Intrinsic damage characteristics for recycled crumb rubber concrete subjected to uniaxial pressure employing cohesive zone model. *Construction and Building Materials*, 317:125773. https://doi.org/10.1016/j.conbuildmat.2021.125773

Hall MR, Najim KB, 2014. Structural behaviour and durability of steel-reinforced structural plain/self-compacting rubberised concrete (PRC/SCRC). *Construction and Building Materials*, 73:490-497. https://doi.org/10.1016/j.conbuildmat.2014.09.063

Huang L, Chi Y, Xu LH, et al., 2019a. A thermodynamics-based damage-plasticity model for bond stress-slip relationship of steel reinforcement embedded in fiber reinforced concrete. *Engineering Structures*, 180:762-778. https://doi.org/10.1016/j.engstruct.2018.11.070

Huang L, Ye HL, Chu SH, et al., 2019b. Stochastic damage model for bond stress-slip relationship of reinforcing bar embedded in concrete. *Engineering Structures*, 194:11-25. https://doi.org/10.1016/j.engstruct.2019.05.053

Ka SB, Han SJ, Lee DH, et al., 2018. Bond strength of reinforcing bars considering failure mechanism. *Engineering Failure Analysis*, 94:327-338. https://doi.org/10.1016/j.engfailanal.2018.08.008

Kammash KNA, Al-Quraishi H, Abdul-Husain ZA, 2022. The behavior of bond strength between rebar and concrete in rubberized concrete. *Journal of Engineering*, 28(8):83-92. https://doi.org/10.31026/j.eng.2022.08.06

Karunarathna S, Ngo T, Linforth S, et al., 2022. Evaluation of the effect of recycled rubber aggregate size on concrete for sustainable applications of rubberised concrete in impact resistant structures: experimental and numerical study. *Journal of Cleaner Production*, 374:133648. https://doi.org/10.1016/j.jclepro.2022.133648

Li DD, Gravina R, Zhuge Y, et al., 2020. Bond behaviour of steel-reinforcing bars in crumb rubber concrete (CRC). *Australian Journal of Civil Engineering*, 18(1):2-17. https://doi.org/10.1080/14488353.2019.1680073

Li H, Ping KL, Chen WM, et al., 2024. Bonding performance between steel bar and rubberized concrete under different loading rates. *Journal of Changjiang River Scientific Research Institute*, 41(9):161-168 (in Chinese). https://doi.org/10.11988/ckyyb.20230437

Li XP, Zhao J, Zhang XC, 2021. A mechanical bond model for reinforcing bar in concrete subjected to monotonic and reversed cyclic loading. *Journal of Building Engineering*, 44:102912. https://doi.org/10.1016/j.jobe.2021.102912

Liu BD, Zhang LL, Feng MY, et al., 2023. Experimental study of rubber-concrete-filled CST composite column under axial compression. *International Journal of Steel Structures*, 23(1):247-262. https://doi.org/10.1007/s13296-022-00692-1

Liu J, Xu WT, Li GS, et al., 2025. Performance and applications of polymer fiber rubber-reinforced concrete in civil engineering: a state-of-the-art review. *Polymers*, 17(7):970. https://doi.org/10.3390/polym17070970

Lu SW, Yang JL, Wang JZ, et al., 2024. Behavior of steel tubed rubberized geopolymer concrete columns under axial compression: experimental study and analytical modeling. *Engineering Structures*, 302:117389. https://doi.org/10.1016/j.engstruct.2023.117389

Mishra S, Panda S, Bhowmik D, et al., 2026. Experimental and analytical evaluation of crumb rubber concrete with multi-blended industrial waste aggregate and SCMs: strength, durability, microstructure, and ML prediction. *Construction and Building Materials*, 516:145677. https://doi.org/10.1016/j.conbuildmat.2026.145677

MOHURD (Ministry of Housing and Urban-Rural Development of the People's Republic of China), AQSIQ (General Administration of Quality Supervision, Inspection and Quarantine of the People's Republic of China), 2011. Technical Code for Safety Appraisal of Engineering Structural Strengthening Materials, GB 50728-2011. National Standards of the People's Republic of China (in Chinese).

Pham TM, Chen WS, Khan AM, et al., 2020. Dynamic compressive properties of lightweight rubberized concrete. *Construction and Building Materials*, 238:117705. https://doi.org/10.1016/j.conbuildmat.2019.117705

Raffoul S, Garcia R, Pilakoutas K, et al., 2016. Optimisation of rubberised concrete with high rubber content: an experimental investigation. *Construction and Building Materials*, 124:391-404. https://doi.org/10.1016/j.conbuildmat.2016.07.054

Reinhardt HW, Cornelissen HAW, Hordijk DA, 1986. Tensile tests and failure analysis of concrete. *Journal of Structural*

Engineering, 112(11):2462-2477. https://doi.org/10.1061/(ASCE)0733-9445(1986)112:11(2462)

RILEM TC, 1994. RC 6 Bond Test for Reinforcement Steel. 2. Pull-Out Test. E & FN SPON, London, UK.

Romanazzi V, Leone M, Tondolo F, et al., 2021. Bond strength of rubberized concrete with deformed steel bar. *Construction and Building Materials*, 272:121730. https://doi.org/10.1016/j.conbuildmat.2020.121730

Sienkiewicz M, Janik H, Borzędowska-Labuda K, et al., 2017. Environmentally friendly polymer-rubber composites obtained from waste tyres: a review. *Journal of Cleaner Production*, 147:560-571. https://doi.org/10.1016/j.jclepro.2017.01.121

Tan X, Xing JL, Wang Y, et al., 2026. Explainable machine learning for predicting compressive strength of rubberized concrete: SHAP interpretation, lifecycle assessment, and design recommendations. *Journal of Cleaner Production*, 538:147338. https://doi.org/10.1016/j.jclepro.2025.147338

Tang SW, Yao Y, Andrade C, et al., 2015. Recent durability studies on concrete structure. *Cement and Concrete Research*, 78:143-154. https://doi.org/10.1016/j.cemconres.2015.05.021

Topçu IB, 1995. The properties of rubberized concretes. *Cement and Concrete Research*, 25(2):304-310. https://doi.org/10.1016/0008-8846(95)00014-3

Turatsinze A, Garros M, 2008. On the modulus of elasticity and strain capacity of self-compacting concrete incorporating rubber aggregates. *Resources, Conservation and Recycling*, 52(10):1209-1215. https://doi.org/10.1016/j.resconrec.2008.06.012

Velegrakis AF, Ballay A, Poulos S, et al., 2010. European marine aggregates resources: origins, usage, prospecting and dredging techniques. *Journal of Coastal Research*, (51): 1-14.

Wang JZ, Yang L, Yang JL, 2020. Bond behavior of epoxy-coated reinforcing bars with seawater sea-sand concrete. *Structural Journal*, 117(4):193-208. https://doi.org/10.14359/51723510

Wang JZ, Xiao FD, Yang JL, 2023. Experimental study on bond behavior between epoxy-coated reinforcement (ECR) and seawater sea-sand concrete (SSC) under FRP-steel confinement. *Construction and Building Materials*, 385: 131426. https://doi.org/10.1016/j.conbuildmat.2023.131426

Wang JZ, Xiao FD, Yang JL, 2024. Bond behavior of stainless steel reinforcement and seawater sea-sand concrete under FRP-steel confinement. *Journal of Materials in Civil Engineering*, 36(3):04023605. https://doi.org/10.1061/JMCEE7.MTENG-16517

Xiao FD, Chen SK, Chen KH, et al., 2025a. Bond behavior of stainless steel (SS) rebar to seawater sea-sand concrete (SSC): experiments and modeling. *Engineering Structures*, 330:119960. https://doi.org/10.1016/j.engstruct.2025.119960

Xiao FD, Wang WX, Yang JL, et al., 2025b. A fractal dimension-modified stochastic damage model for bond-slip responses of corroded steel rebar embedded in different types of geopolymer concrete. *Engineering Structures*, 333:120168. https://doi.org/10.1016/j.engstruct.2025.120168

Xiao FD, Li Q, Lu SW, et al., 2026. Bond failure of corroded rebar embedded in rubberized geopolymer concrete: experimental evaluation. *Construction and Building Materials*, 519: https://doi.org/10.1016/j.conbuildmat.2026.145922

Xu ZW, Yan DM, 2023. An improved prediction for bond strength of deformed bars in concrete externally confined with fiber-reinforced polymer. *Materials Journal*, 120(6): 19-32. https://doi.org/10.14359/51739144

Xu ZW, Liu Y, Zeng Q, et al., 2022. An improved model for predicting bond strength of deformed rebars in concrete with stirrups. *Engineering Fracture Mechanics*, 276:108893. https://doi.org/10.1016/j.engfracmech.2022.108893

Xu ZW, Chen SK, Qian H, et al., 2023. Analytical bond strength of deformed bars in concrete confined with transverse reinforcement and FRP. *Engineering Structures*, 280:115594. https://doi.org/10.1016/j.engstruct.2023.115594

Yan DM, Qiu YL, Gao RF, et al., 2025. Evolution of waterproof performance, mechanical properties, and microstructure in hydrophobically-modified geopolymer concrete during dry-wet cycles. *Journal of Zhejiang University-Science A*, 26(3):194-211. https://doi.org/10.1631/jzus.A2400020

Zhang X, Dong W, Lv CM, et al., 2019. Analytical approach to modeling the effect of transverse reinforcements on the bond strength of deformed bars. *Journal of Structural Engineering*, 145(6):04019046. https://doi.org/10.1061/(ASCE)ST.1943-541X.0002293

Zhang ZC, Zhou DD, He J, et al., 2023. Insight into the impact of industrial waste co-disposal with MSW on groundwater contamination at the open solid waste dumping sites. *Chemosphere*, 344:140429. https://doi.org/10.1016/j.chemosphere.2023.140429

Zhao WP, Zhu BR, 2018. Theoretical model for the bond-slip relationship between ribbed steel bars and confined concrete. *Structural Concrete*, 19(2):548-558. https://doi.org/10.1002/suco.201700008

Electronic supplementary materials

Tables S1–S3